



# Quantitative investigation of fracture interaction by evaluating fracture curvature during temporarily plugging staged fracturing

Bo Wang<sup>a,b,c</sup>, Fujian Zhou<sup>a,b,\*</sup>, Yushi Zou<sup>a,b</sup>, Tianbo Liang<sup>a,b</sup>, Daobing Wang<sup>a,b</sup>, Yanpeng Xue<sup>d</sup>, Liyang Gao<sup>a</sup>

<sup>a</sup> State Key Laboratory of Petroleum Resources and Prospecting, China University of Petroleum, Beijing, 102249, China

<sup>b</sup> Unconventional Natural Gas Research Institute, China University of Petroleum, Beijing, 102249, China

<sup>c</sup> Beijing Branch, Research Institute of Petroleum Exploration and Development, China National Petroleum Cooperation, Beijing, 100083, China

<sup>d</sup> Tarim Research Institute of Petroleum Engineering, China National Petroleum Corporation, Korla, 841000, China

## ARTICLE INFO

### Keywords:

Temporarily plugging staged fracturing

XFEM-Based CZM

Plugging efficiency

Propagation path

## ABSTRACT

Temporarily plugging staged fracturing (TPSF) technique has been successfully applied in unconventional reservoirs. This paper quantitatively investigates fracture interaction between previous and subsequent fractures during TPSF through numerical experiments. Using XFEM-based CZM (the cohesive zone model based on the extended finite element method), a 2D fully fluid-solid coupling model is established to perform the investigation. Typically, the concept of “turning angle” is proposed to quantify the degree of fracture interaction under different conditions. Moreover, the opening of the previously created fracture is simulated by truss model, which indicates truss elements distributed on the fracture surfaces; the effects of formation heterogeneity are investigated by changing rock mechanical properties surrounding the subsequent fractures. Simulation results reveal that the previously created and propped fracture will generate induced stresses, which cause the subsequent fracture to propagate with curvature. Factors influencing the subsequent fracture propagation curvature during TPSF, are sorted by sensitivity (strong to weak): plugging efficiency, Young's modulus, percent of initial aperture propped, fracture spacing, horizontal stress contrast, rock tensile strength, and formation permeability. The investigations provide a deep understanding of fracture interaction between previous and subsequent fractures during TPSF.

## 1. Introduction

Multi-stage fracturing is an effective way to develop unconventional reservoirs due to the high contact area with formations (Wang et al., 2015a, 2015b). The conventional multi-stage fracturing techniques include ball-activated sliding-sleeve staged fracturing (Rytlewski et al., 2008), multistage fracturing using plug and perf systems (Aviles et al., 2015) and hydro-jet staged fracturing technology combined with coiled tubing (Gensheng et al., 2012); however, for deep formations, they are relatively expensive and risky. Temporarily plugging staged fracturing (TPSF), using diverting agents to plug the previously created fractures, has developed rapidly in the past five years; by comparison, it is more convenient, economical and safe to isolate the lateral. During TPSF, fracture interaction is important for fracture design, for it determines how many effective fractures (with small curvature and no tip screen out) can be created and how much diverting material should be injected (Rahim et al., 2017; Senters et al., 2018).

Up to now, fracture interaction has been investigated through various models. Xu et al. (2010), Meyer and Bazan (2011), and Weng et al. (2011) proposed a wire model, a discrete fracture network model and the unconventional fracture model, respectively, to investigate multiple fracture propagation in naturally fractured formations. They concluded that the geometry of multiple fractures are strongly influenced by mechanical interaction between fractures and the key factor is fracture spacing. Nagel et al. (2013), Zou et al. (2016) and Yushi et al. (2016, 2017) used discrete-element method to simulate multiple fracture propagation. Dahi-Taleghani and Olson (2011, 2014) simulated multiple fracture geometry based on the extended finite element method (XFEM). Wu and Olson (2013, 2015, 2016, 2017) developed a novel fracture propagation model using a simplified 3D displacement discontinuity method (DDM) to simulate multiple fracture propagation. They emphasized that fracture interaction and the intersection of the hydraulic and natural fracture highly influence fracture geometry, and the physical mechanisms of complex fracture geometry were revealed,

\* Corresponding author. State Key Laboratory of Petroleum Resources and Prospecting, China University of Petroleum, Beijing, 102249, China.

E-mail address: [zhoufj@cup.edu.cn](mailto:zhoufj@cup.edu.cn) (F. Zhou).

<https://doi.org/10.1016/j.petrol.2018.08.038>

Received 31 March 2018; Received in revised form 16 June 2018; Accepted 13 August 2018

Available online 23 August 2018

0920-4105/ © 2018 Elsevier B.V. All rights reserved.

as well as insights for operators to design fracturing treatments were offered. In ABAQUS (a commercial finite element software), Haddad and Sepehrnoori (2014) simulated multiple fracture propagation in quasi-brittle shale formation using characterized cohesive layer. They concluded that fracture interaction majorly affects fracture length, height, aperture, injection pressure and the connection to the injection spot. Using XFEM-based CZM (the cohesive zone model based on XFEM) in Abaqus, Liu and Wang et al. (2016) established a 2D model to optimize the spacing of sequential and simultaneous fracturing. They concluded that the optimal spacing decreases with in-situ stress contrast, while it is not sensitive to Young's modulus. Haddad and Sepehrnoori (2016) simulated 3-fracture propagation in a single 3D layer using XFEM-based CZM. They found that fracture interaction causes fractures to coalesce, grow parallel or diverge depending on cluster spacing.

However, the existing investigations of fracture interaction just provided a qualitative knowledge through the resultant fracture geometries. It demonstrates fracture interaction will influence fracture geometry, while which are the key factors influencing fracture interaction has not been reported. Moreover, during TPSF, multiple fractures will not initiate and propagate simultaneously due to reservoir heterogeneities and fracture interaction, instead, fractures will initiate and propagate one by one. After plugged by diverting agents, the previous fractures will be propped by fracturing fluids (Wang et al., 2018), this is quite different from the simultaneous propagation of multiple fractures. Therefore, quantitative and systematic investigations of fracture interaction during TPSF should be carried out further carried.

In this study, fracture interaction during TPSF has been investigated quantitatively and systematically through numerical simulation. Using XFEM-based CZM, a 2D fluid-solid coupling model is established to perform the investigations. "Turing angle" is proposed to represent the subsequent fracture curvature. At the beginning, this paper presents the stress fields and the rock displacement fields induced by the previously created and propped fracture, as well as calculated the injection pressure of both previously created and subsequently created fractures; then this paper investigates the influences of operation parameters (plugging efficiency and width of the previously created fracture) on the propagation path and geometry of the subsequent fractures; after that, this paper investigates the influences of reservoir parameters (fracture spacing, formation permeability and horizontal stress contrast) in homogeneous formations; in the end, this paper investigates the effects of rock mechanical parameters (Young's modulus and rock tensile strength) in heterogeneous formations.

## 2. Mechanisms of TPSF

TPSF is mainly used in deep horizontal wells because the conventional mechanical isolation methods are dangerous and expensive. During temporarily plugging staged fracturing (TPSF), bridge plugs are used to block a stage. Usually, there are 2–5 perforation clusters existing in one fracturing stage. After injecting fracturing fluids, not all the perforation clusters form efficient fractures due to the differences in fracture initiation pressure and fracture interaction. When the previous fracture propagation is completed, diverting agents are injected into the fracturing fluids and will be carried into the previous fractures, then tight filter cakes will be formed within those fractures. The tight filter cakes prevent the fracturing fluids from entering into the previous fractures. Thus injected fracturing fluids will enhance the wellbore pressure and the subsequent fractures from other perforation clusters in the same stage will initiate and propagate. Compared to the conventional methods, for example, limited entry fracturing or mechanical packer, TPSF can dramatically enhance the perforation cluster efficiency and reduce the number of mechanical packer. Fig. 1 gives the schematic of the process of TPSF (assuming  $p_{wf1} < p_{wf2} < p_{wf3} < p_{wf4}$ ). In Fig. 1a, the horizontal well is isolated at the toe with a packer, then fracturing fluids are injected and the wellbore pressure is enhanced;

when fluid pressure reaches up to  $p_{wf1}$  (i.e., the initiation pressure of Frac. 1), Frac. 1 initiates and propagates to a long distance. In Fig. 1b, Frac. 1 is plugged with self-degradable diverting agents and the subsequent injection fluids increase wellbore pressure gradually; when wellbore pressure reaches  $p_{wf2}$ , Frac. 2 initiates and propagates (neglecting fracture curvature). In Fig. 1c and d, Frac. 3 initiates and propagates after Frac. 2 is plugged, then Frac. 4 initiates and propagates after Frac.3 is plugged. When the entire lateral is fractured, diverting agents dissolve and flow out of the wellbore.

## 3. Fracture propagation model

To simulate fracture propagation geometry, various factors need to be taken into consideration, including fracturing fluid flowing within fractures and in the surrounding porous media, fluid leaking off into the formation, the rock deformation, and the fracture propagation resistance (Liu and Forouzanfar, 2017). More difficultly, these factors are fully coupled at the same time. Specifically, the flowing pressure within fractures influences the fluid leak-off rate; rock deformation impacts the matrix porosity and formation permeability; fracture aperture strongly depends on the fluid flowing pressure; and induced stresses resulting from the previous fractures highly impact the subsequent fracture propagation (Feng and Gray, 2017).

This paper considered all above-mentioned factors, and the extended finite element (XFEM) is used to describe fracture characteristics, as well as the cohesive zone model is applied to determine fracture initiation and propagation. Cohesive zone model (CZM) idealizes complex fracture mechanism using a macroscopic "cohesive law", which is the relation between the traction across the interface and the separation. Cohesive zone model includes damage initiation and evolution conditions. Moreover, this model avoids both pressure and stress singularities at fracture tips. The adoption of CZM in finite element (FEM) simulate fracture propagation along a pre-defined path by inserting the pre-defined planar cohesive layers (Haddad and Sepehrnoori, 2015). The extended finite element method (XFEM) can simulate the fracture propagation along arbitrary paths independent of the mesh. XFEM incorporates the discontinuous geometry, the fracture, and the discontinuous field by enriching the finite element basis functions. The enriched basis functions include Heaviside function and crack tip asymptotic function, the former represents a displacement jump across the fracture surface, the later represents the crack tip singularity. XFEM-based CZM refers to integrating CZM as the segmental contact interaction model with a fully coupled pore pressure-displacement model based on XFEM. XFEM-based CZM can simulate the fracture initiation and propagation along an arbitrary, solution-dependent path (Haddad and Sepehrnoori, 2016).

### 3.1. Fluid flow and rock deformation

#### 3.1.1. Fluid flow within fractures

Assuming the fracturing fluid is the incompressible and Newtonian type, thus the tangential flow rate  $q_f$  within the fracture can be determined by the lubrication equation (Zielonka et al., 2014)

$$q_f = -\frac{w^3}{12\mu} \nabla p_f \quad (1)$$

Where  $q_f$  is the average fluid velocity,  $m^2/s$ ;  $w$  is the fracture aperture,  $m$ ;  $\mu$  is the fluid viscosity,  $cp$ ;  $p_f$  is the fluid pressure within the fracture,  $Pa$ .

The fluid mass conservation law can be described as (Zielonka et al., 2014)

$$\nabla q_f - \frac{\partial w}{\partial t} + q_b + q_t = 0 \quad (2)$$

Where  $q_b$ ,  $q_t$  are the normal flow velocity at the bottom fracture surface and at the top fracture surface, respectively,  $m/s$ .

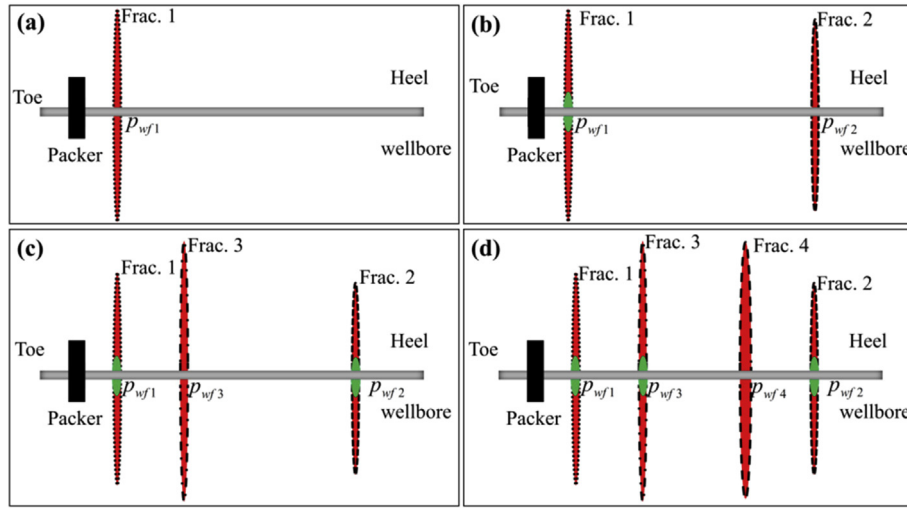


**Fig. 1.** The process of temporarily plugging staged fracturing;  $p_{wf1}$ ,  $p_{wf2}$ ,  $p_{wf3}$ ,  $p_{wf4}$  are the initiation pressure of Frac. 1, Frac. 2, Frac. 3 and Frac. 4, respectively. (Assuming  $p_{wf1} < p_{wf2} < p_{wf3} < p_{wf4}$ ).

The fluid leakoff can be determined by the normal flow equation (Zielonka et al., 2014)

$$\begin{aligned} q_b &= c_b(p_f - p_w) \\ q_t &= c_t(p_f - p_w) \end{aligned} \quad (3)$$

Where  $c_b$ ,  $c_t$  are the leak off coefficient at the bottom fracture surface and at the top fracture surface, respectively, m/s/Pa;  $p_w$  is the pore pressure of the formation close to the fracture, Pa.

### 3.1.2. Fluid flow in porous media

The continuity equation of fluid can be written as (Zhang et al., 2010)

$$\frac{1}{J} \frac{\partial}{\partial t} (J \rho_w n_w) + \frac{\partial}{\partial x} (\rho_w n_w v_w) = 0 \quad (4)$$

Where  $J$  is the volume change ratio of porous media, dimensionless;  $\rho_w$  is fluid density, kg/m<sup>3</sup>;  $n_w$  is the porosity ratio, dimensionless;  $v_w$  is the seepage velocity of the fluid, m/s;  $x$  is space vector, m.

According to Darcy's law, the liquid flow in porous media can be expressed by (Zhang et al., 2010):

$$v_w = -\frac{1}{n_w g \rho_w} \mathbf{k} \cdot (\mathbf{p}_w - \rho_w \mathbf{g}) \quad (5)$$

Where  $\mathbf{k}$  is the matrix permeability tensor of the porous media, m/s;  $\mathbf{g} = -g \partial z / \partial x$  is the vector of the gravitational acceleration, m/s<sup>2</sup>.

### 3.1.3. Rock deformation

Based on the virtue work principle, the equilibrium equation under its current configuration can be described by (Zhang et al., 2010)

$$\int_V (\bar{\boldsymbol{\sigma}} - p_w \mathbf{I}) \delta \boldsymbol{\varepsilon} dV = \int_S \mathbf{t} \cdot \delta \mathbf{v} dS + \int_V \mathbf{f} \cdot \delta \mathbf{v} dV \quad (6)$$

Where  $\mathbf{t}$  is the surface traction vector per unit area, N/m<sup>2</sup>;  $\mathbf{f}$  is the body force vector per unit volume, N/m<sup>3</sup>;  $\mathbf{I}$  is identity matrix, dimensionless;  $\delta \boldsymbol{\varepsilon}$  is the matrix of virtual strain rate, s<sup>-1</sup>;  $\delta \mathbf{v}$  is the matrix of virtual velocity, m/s.  $\bar{\boldsymbol{\sigma}}$  is the matrix of effective stress, Pa.

### 3.2. XFEM approximation

XFEM was first proposed by Belytschko and Black (1999); this method allows discontinuities (fractures) to cross elements and removes the requirement of mesh refinement (Dahi-Taleghani and Olson, 2014). Fractures are ensured by the special enriched functions in conjunction with additional degrees of freedom; the special enriched functions are

composed of asymptotic functions and discontinuous functions; and asymptotic functions are used to capture the singularities close to the fracture tips, while discontinuous functions are used to express the displacement jump across the fracture surfaces (Belytschko and Black, 1999). With the partition of unity enrichment, the displacement vector  $\mathbf{u}$  is approximated by (Fries and Baydoun, 2012)

$$\mathbf{u} = \sum_{I=1}^N N_I(\mathbf{x}) [\mathbf{u}_I + H(\mathbf{x}) \mathbf{a}_I + \sum_{\alpha=1}^4 F_{\alpha}(\mathbf{x}) \mathbf{b}_I^{\alpha}] \quad (7)$$

Where  $N_I(\mathbf{x})$  is the usual nodal shape function;  $\mathbf{u}_I$  is the usual nodal displacement vector,  $\mathbf{a}_I$  is the nodal enriched degree of freedom vector,  $H(\mathbf{x})$  is the discontinuous jump function across the fracture surfaces,  $\mathbf{b}_I^{\alpha}$  is the nodal enriched degree of freedom vector,  $F_{\alpha}(\mathbf{x})$  is the elastic asymptotic crack-tip function. On the right side of the function (7), the first term  $\mathbf{u}_I$  is valid for all the nodes. The second term  $H(\mathbf{x}) \mathbf{a}_I$  is used for the nodes, of which the shape function is partitioned by the crack interior. The third term  $\sum_{\alpha=1}^4 F_{\alpha}(\mathbf{x}) \mathbf{b}_I^{\alpha}$  is applicable for the nodes, of which the shape function is partitioned by the crack tip. The equations for calculating  $H(\mathbf{x})$  and  $F_{\alpha}(\mathbf{x})$  are given in several papers (Dahi-Taleghani and Olson, 2014; Haddad and Sepehrnoori, 2016).

### 3.3. Cohesive zone method

The cohesive zone method (CZM) consists of two parts: a damage initiation criterion and a damage evolution law.

#### 3.3.1. Damage initiation criterion

Damage initiation is the beginning of material degradation and begins when the stresses or strains satisfy initiation criteria. According to Haddad and Sepehrnoori (2016), the maximum principal stress criterion used in XFEM-based CZM can be expressed by

$$f = \left\{ \frac{\langle \sigma_{\max} \rangle}{\sigma_{\max}^0} \right\} \quad (8)$$

Where  $f$  is the maximum principal stress ratio, dimensionless;  $\sigma_{\max}$  and  $\sigma_{\max}^0$  are the maximum principal stress and maximum allowable principal stress, respectively, MPa; The symbol  $\langle \rangle$  represents the Macaulay bracket with the usual interpretation (i.e.,  $\langle \sigma_{\max} \rangle = 0$  if  $\sigma_{\max} < 0$  and  $\langle \sigma_{\max} \rangle = \sigma_{\max}$  if  $\sigma_{\max} \geq 0$ ), which signifies that a purely compressive stress state will not initiate damage, and damage initiates as  $f$  reaches a value of one; this indicates fracture propagates perpendicular to the maximum local tensile stress direction all the way.

### 3.3.2. Damage evolution law

The damage evolution law describes the degradation rate of cohesive stiffness once the corresponding initiation criterion is reached. When  $f$  reaches a value of one, the stress components of the traction-separation model are expressed by (Zielonka et al., 2014)

$$\mathbf{t} = \begin{cases} (1 - D)\bar{\mathbf{t}} & \text{damage initiated} \\ \bar{\mathbf{t}} & \text{no damage occurs} \end{cases} \quad (9)$$

Where  $\mathbf{t}$  is the real stress vector, Pa;  $\bar{\mathbf{t}}$  is the stress vector predicted by the linear T-S (traction-separation) roles for local strains without damage, Pa;  $D$  is the damage factor, dimensionless, increase from 0 to 1 as the separation between the fracture surfaces becomes large.

During fracture propagation, the Benzeggagh-Kenane (BK) criterion is used to determine the mixed-mode damage evolution (Benzeggagh and Kenane, 1996). The BK law model is described by

$$G_{equivC} = G_{IC} + (G_{IIC} - G_{IC}) \left( \frac{G_{IIC} + G_{IIIC}}{G_{IC} + G_{IIC} + G_{IIIC}} \right) \quad (10)$$

Where  $G_{equivC}$  is the calculated equivalent fracture energy release rate, N/mm;  $G_{IC}$  is the Model I (tension failure) fracture energy release rate, N/mm;  $G_{IIC}$  is the Model II (shear failure under sliding) fracture energy release rate, N/mm;  $G_{IIIC}$  is the Model III (shear failure under tearing) fracture energy release rate, N/mm; in BK roles,  $G_{IIC}$  equals to  $G_{IIIC}$ . In the simulation model, when  $G_{equivC}$  reaches to  $G_C$ , the fracture will propagate orthogonally to the maximum principal stress direction based on the maximum principle criterion. In ABAQUS, tensile stress is positive, and compressive stress is negative.

## 4. Model construction and verification

### 4.1. Model construction

A case of 3-fracture is simulated (Fig. 2a). In Fig. 2b, the diameter of the whole model is 1000 m and the enriched zone (the middle green region) is a square with 200 m long. In Fig. 2c, zero-displacement and constant pore pressure boundary conditions are applied to the outer semicircle edge "ACB"; the symmetric boundary condition is defined on the edge AOB. The middle enriched zone (i.e., fracture propagation region) is refined to improve the calculation accuracy. The whole model has 162299 nodes and 161901 elements (including pore pressure element (CPE4P) and truss element (T2D2)). In Fig. 2d, initial cracks are preset to simulate perforations and receive fracturing fluids. The fracture spacing of the base case is 20 m. This paper defines the left fracture

as Frac. 1, the middle fracture as Frac. 2, the right fracture as Frac. 3. During simulation, Frac. 2 propagates firstly for 1200 s, after that, Frac. 2 is plugged by diverting agents and Fracs. 1&3 begin to initiate and propagate. During the propagation of Fracs. 1&3, Frac. 2 is propped by truss elements. Truss elements should be added as follows. To begin with, we propagate Frac. 2 (the previous fracture) and determine the propagation path of Frac. 2, then we exact the nodes surrounding Frac. 2 surfaces and build truss elements; after that, we re-propagate Frac. 2 under the identical condition; in the end, we activate the truss elements distributed on Frac. 2 surfaces and propagate Frac. 1&3.

### 4.2. Model verification

The reliability and accuracy of XFEM-based CZM on modeling multiple fracture propagation have been verified by previous studies (Wang et al., 2016; Haddad and Sepehrmoori, 2016; Liu et al., 2015, 2017). In this part, two fracture propagation with the spacing of 10 m is simulated using the model in Fig. 2. Then the simulation results are compared with those from the Unconventional Fracture Model (UFM) (Wu et al., 2012). Unconventional Fracture Model, a complex fracture network model, has been developed by Weng et al. (2011) and Kresse et al. (2011). This model simulates the fracture propagation, rock deformation, and fluid flow in the complex fracture network. Moreover, this model solves the fully coupled problem of fluid flow in the fracture network and the elastic deformation of the fractures, which has similar assumptions and governing equations as conventional pseudo-3D fracture models. The input parameters are listed in Table 1 and the comparing results are given in Fig. 3. It shows that both fracture propagation path and fracture width vs. length are in good agreement, respectively.

On the other hand, in order to verify simulation results from XFEM-based CZM are promising reflections of the actual experiments, a 2D model was established to simulate near-wellbore fracture propagation with directional perforations (illustrated in Fig. 4). The perforation phase angle is 60°, and Table 2 gives the same input parameters as the reported laboratory fracturing test (Abass et al., 1994). Fig. 5 gives the fracture propagation path. It shows that the fracture trajectories from the numerical simulation model and the laboratory experiments match very well.

## 5. Results and discussion

The effects of Frac. 2 (the previous fracture) on the propagation

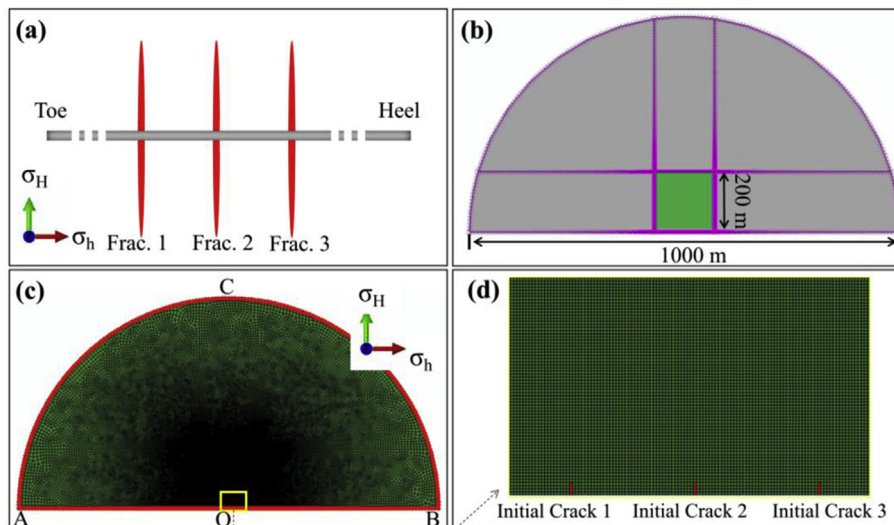


Fig. 2. The simulation model. (a) The physical model of three fractures along the lateral; (b) The geometry of the simulation model; (c) Model with mesh; (d) Three initial cracks in the middle region.



**Table 1**  
Input parameters used for verification (Wu et al., 2012).

PARAMETER	VALUES
Young's modulus, $E$ (GPa)	30
Poisson's ratio, $\nu$ (dimensionless)	0.35
Minimum principle horizontal stress, $\sigma_h$ (MPa)	46.7
Maximum principle horizontal stress, $\sigma_H$ (MPa)	47.6
Injection rate, $Q$ (m <sup>3</sup> /min)	3.6
Permeability, $k$ (mD)	0.5
Void ratio, $n_w$ (dimensionless)	0.1
Fluid viscosity, $\mu$ (mPa·s)	1180
Damage initiation stress (equivalent to rock tensile strength), $\sigma_{omax}$ (MPa)	2
Critical energy release rate, $G_{IC}$ and $G_{IIC}$ (kJ/m)	30
Leakoff coefficient (m <sup>3</sup> /kPa·s)	$5.879 \times 10^{-10}$

curvature and width of Fracs. 1&3 (the subsequent fractures) under various conditions are primarily focused in this paper, and the input parameters of the simulation cases are listed in Table 3.

The simulation results are briefly explained by use of the relative net pressure  $R_n$ , defined by Olson and Dahi Taleghani (2009),

$$R_n = \frac{P_f - \sigma_h}{\sigma_H - \sigma_h} \quad (11)$$

Where  $R_n$  is the relative net pressure, dimensionless;  $P_f$  is fluid pressure within the fracture, MPa;  $\sigma_H$  is the maximum horizontal principal stress, MPa;  $\sigma_h$  is the minimum horizontal principal stress, MPa.

The numerator refers to the net pressure and the denominator refers to the horizontal differential stress. According to Olson and Dahi Taleghani (2009), if the relative net pressure of  $R_n$  is much larger than unity, the fracture is less constrained to propagate in the direction of maximum horizontal stress and tends to propagate along the current direction. While for a smaller  $R_n$ , horizontal differential stress dominates the fracture geometry and fracture tend to divert to the direction of the local maximum horizontal stress. When the initial horizontal stress contrast is small, fracture propagation direction is susceptible to induced stresses resulting from fracture interaction.

### 5.1. Stresses and rock displacement fields induced by propped fractures

This paper defines the base case: fracture spacing is 20 m and the input parameters are listed in Table 3. Fig. 6a gives the rock displacement fields altered by Frac. 2 (i.e., the previously created fracture). It shows that the opening of Frac. 2 directly squeezes the rock and induces rock displacement, which increases the compressional stress parallel to the direction of the minimum horizontal stress (Fig. 6c) (Feng et al., 2015, 2016). In Fig. 6d, the movement of the Frac.3-left surface is much smaller than that of Frac. 3-right surface as a result of the compressional

stress arising from Frac. 2. Besides, the enhancement of compressional stress decreases the horizontal differential stress and changes the direction of maximum-circumferential-stress. Fracs. 1&3 propagate straightly in the beginning and divert afterwards. In the beginning, the injection pressure is large enough to promote Fracs. 1&3 to propagate along the current direction (shown in Fig. 7); while after the injection pressure reduces, the local stress fields dominate the propagation direction, thus Fracs. 1&3 propagate with curvature.

### 5.2. The effects of operational parameters

#### 5.2.1. Plugging efficiency

Fracture tends to initiate and propagate from perforations with less restriction. Formation heterogeneity and induced stresses caused by previous fracture lead to the limitation of fracture number and the fracture immature propagation (Dahi-Taleghani and Olson, 2011; Li and Misra, 2017a). It is efficient to plug the previously created fracture by diverting agents and divert subsequent fluid into untreated perforation clusters (Rahim et al., 2017; Weddle et al., 2017). This part investigates the effects of plugging efficiency of the previously created fractures. Plugging efficiency represents the percent of flow-rate reduction entering into the previous fracture. For example, plugging efficiency of 100% indicates the previous fracture is absolutely plugged and no subsequent fluids flow into it. It is assumed that Frac. 2 propagates firstly and lasted for 1200 s, and then the injection rate flowing into Frac. 2 is reduced to simulate different plugging efficiency (50%, 60%, 80% and 100%, respectively). The effects of Frac. 2 on the propagation path of Fracs. 1&3 (subsequent fractures) are shown in Fig. 8. Fracs. 1&3 propagate more maturely with the increase of plugging efficiency of Frac. 2 because more fracturing fluid is diverted from Frac. 2 into Fracs. 1&3. A series of laboratory experiments on the optimization of diverting agents have been carried out, which ensures the success of perfect plugging efficiency of previous fractures through adjusting loading, particulate size and distribution (Allison et al., 2011; Potapenko et al., 2009; Gomaa et al., 2016a,b).

#### 5.2.2. Propped aperture of previous fractures

Fracture opening directly squeezes the rock perpendicular to the direction of width, which strongly influences the magnitude of fracture interaction (Wang et al., 2009; Wu and Olson, 2016; Cheng et al., 2017). In this part, it is assumed that Frac. 2 (the previous fracture) is plugged completely, thus fracturing fluid in the wellbore would not enter into Frac. 2, meanwhile, fracturing fluid within fracture would not flow out. Influenced by formation permeability, wall-building ability of fracturing fluid, and gel breaking capability of carrier fluid, fracturing fluid within Frac. 2 filtrates into the surrounding rock at different rates, which results in different fluid pressure and aperture of Frac. 2. Truss model (truss elements distributed on fracture surfaces)

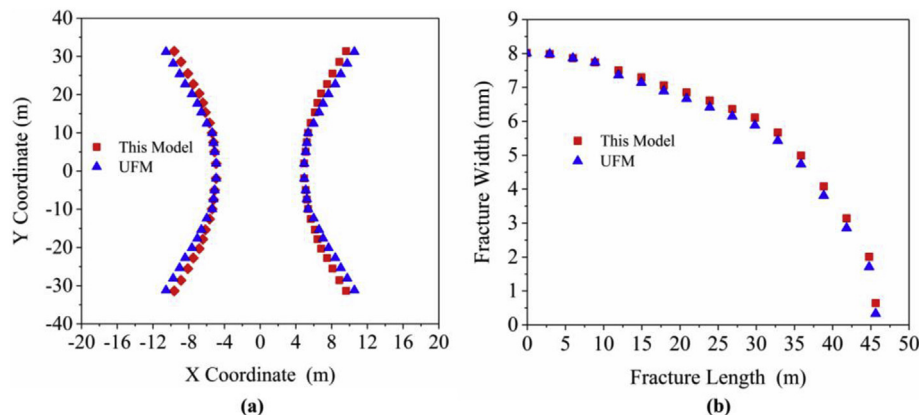


**Fig. 3.** Comparison with published simulation results. (a) Trajectory comparison; (b) Fracture width comparison.

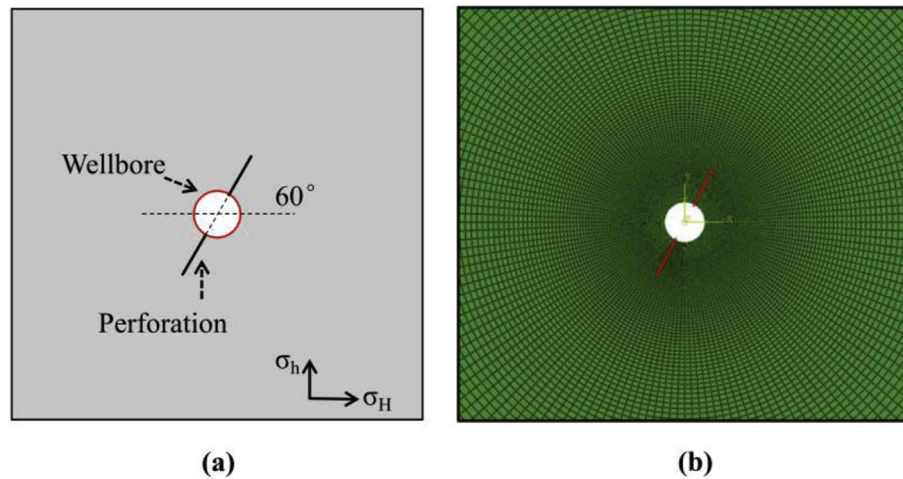


Fig. 4. Schematic and mesh refinement of the simulation model: (a) Model schematic; (b) Mesh refinement.

Table 2

Input parameters of the verification model (Abass et al., 1994).

PARAMETER	VALUES
Young's modulus, $E$ (GPa)	17.4
Poisson's ratio, $\nu$ (dimensionless)	0.228
Minimum principle horizontal stress, $\sigma_h$ (MPa)	9.6
Maximum principle horizontal stress, $\sigma_H$ (MPa)	17.2
Injection rate, $Q$ (m <sup>3</sup> /min)	3.6
Permeability, $k$ (mD)	9.5
Void ratio, $\phi$ (dimensionless)	0.33
Fluid viscosity, $\mu$ (mPa·s)	10
Damage initiation stress (equivalent to rock tensile strength), $\sigma_{omax}$ (MPa)	5.56
Critical energy release rate, $G_{IC}$ and $G_{IIC}$ (kJ/m)	30

with different stiffness is used to prop different aperture of previously created fracture (75%, 80%, 90% and 100% of the initial aperture of Frac. 2, respectively). The simulation results (given in Fig. 9) illustrate that larger propped aperture of Frac. 2 generates greater curvature and slightly narrow width of Fracs. 1&3 as a result of stronger fracture interaction. Furthermore, Frac. 2 has longer length with smaller aperture. The reason is that as the fracture aperture decreases, fracture surfaces squeeze fracturing fluid, which increases fluid pressure within Frac. 2 and propagates Frac. 2 forward slightly (Wu and Olson, 2016; Cheng et al., 2017). It can be concluded that optimizing the aperture of the previous fractures should consider obtaining high fracture-conductivity

Table 3

Input parameters used in the simulation model.

PARAMETER	VALUES
Young's modulus, $E$ (GPa)	40
Poisson's ratio, $\nu$ (dimensionless)	0.2
Minimum principle horizontal stress, $\sigma_h$ (MPa)	57
Maximum principle horizontal stress, $\sigma_H$ (MPa)	60
Initial pore pressure, $p_o$ (MPa)	45
Injection rate, $Q$ (m <sup>3</sup> /min)	4
Permeability, $k$ (mD)	0.01
Void ratio, $\phi$ (dimensionless)	0.1
Fluid viscosity, $\mu$ (cp)	10
Damage initiation stress (equivalent to rock tensile strength), $\sigma_{omax}$ (MPa)	2
Critical energy release rate, $G_{IC}$ and $G_{IIC}$ (N/mm)	30
Leakoff coefficient (m/s/Pa)	$5.879 \times 10^{-10}$

and reducing fracture interaction at the same time.

### 5.3. The effects of reservoir parameters in homogeneous formations

#### 5.3.1. Fracture spacing

During TPSF, fracture initiation position and created sequence depend on the fracture breakdown pressure along the wellbore (Rahim et al., 2017; Weddle et al., 2017), thus fractures are created with various fracture spacing due to irregular initiation positions. Considering

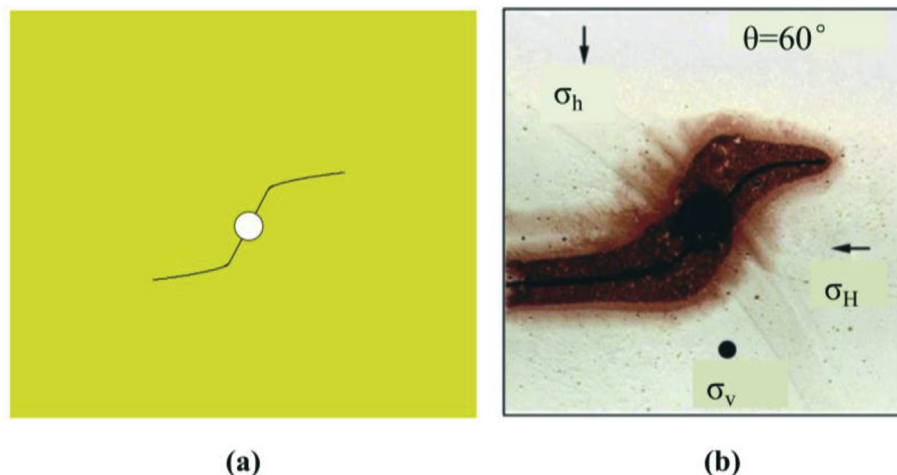


Fig. 5. Comparison of fracture trajectories from simulation and experimental results. (a) Simulation result. (b) Laboratory experimental result (Abass et al., 1994).

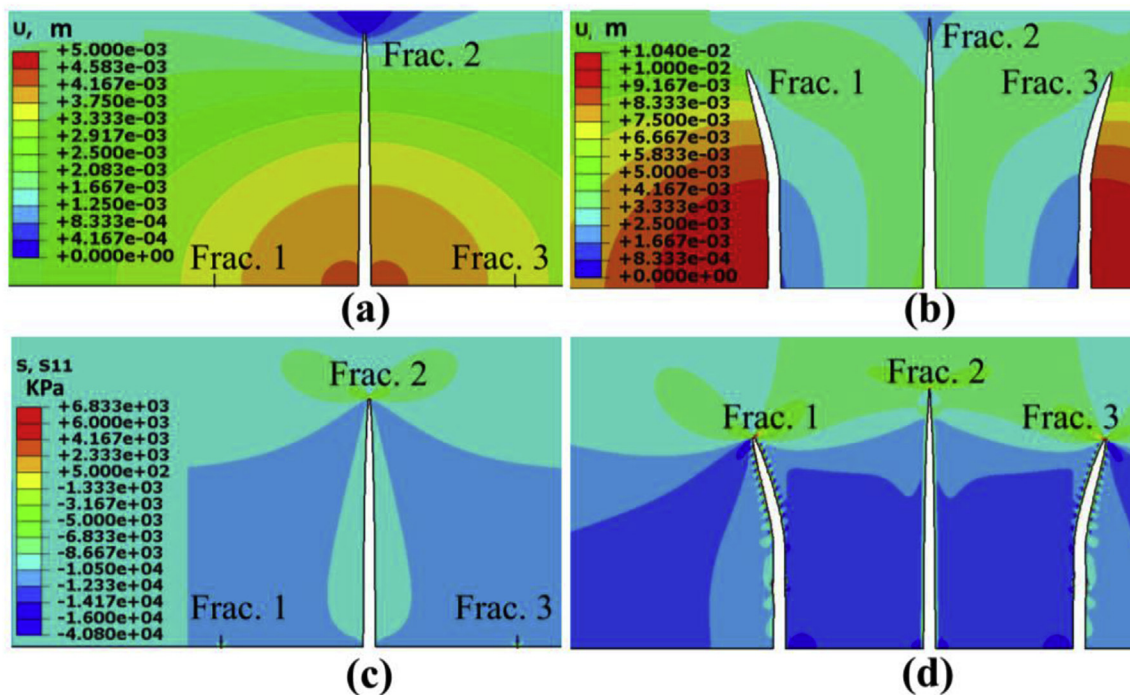


Fig. 6. Stress and rock displacements induced by a propped fracture (“U” represents rock displacement and “s11” represents the stress along the direction of the original minimum horizontal stress). (a) Rock displacement induced by Frac. 2. Red color represents large rock displacement and blue color represents small rock displacement; (b) Rock displacement induced by the three fractures; (c) s11 distribution induced by Frac. 2. Red color represents tensile stress and blue color represents compress stress; (d) s11 distribution induced by the three fractures. (For interpretation of the references to color in this figure legend, the reader is referred to the Web version of this article.)

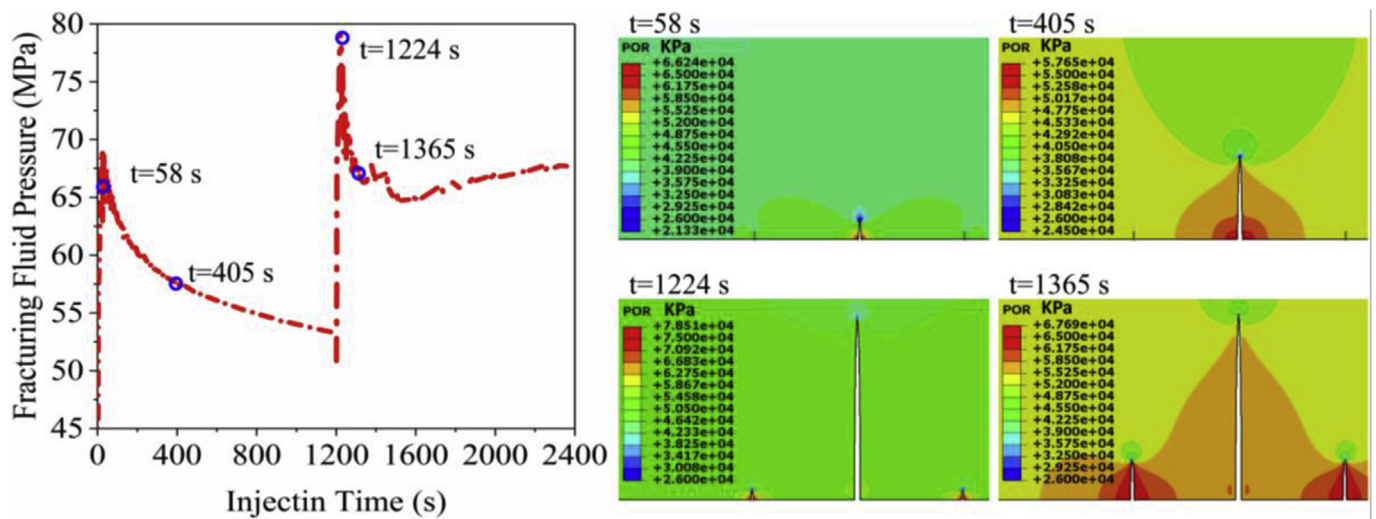


Fig. 7. Left: injection pressure vs. time (0–1200 s: the injection pressure curve of Frac. 2. 1200–2400s: the injection pressure curve of Fracs. 1&3); Right: pore pressure distribution at the certain time (“POR” represents node pore pressure and red color represents large pore pressure). (For interpretation of the references to color in this figure legend, the reader is referred to the Web version of this article.)

mechanical interaction between fractures highly depends on fracture spacing (Liu et al., 2015; Wang et al., 2016), this part simulates four cases with fracture spacing of 12 m, 20 m, 26 m, and 32 m. As presented in Fig. 10, Fracs. 1&3 propagate more straightly with increasing fracture spacing. The reason is that induced stresses caused by Frac. 2 decrease with fracture spacing. Furthermore, it shows that the average aperture of Fracs. 1&3 decreases slightly with fracture spacing because decreased induced stresses lead to smaller propagation resistance, which decreases the fluid pressure within Fracs. 1&3. As for filled treatments, too small fracture spacing cannot be obtained even with a large amount of diverting agents. This can be verified by the

microseismic event distributions during TPSF (Potapenko et al., 2009).

### 5.3.2. Formation permeability

High permeability leads to high fluid leak-off rate (Liang et al., 2017a), which influences fracture aperture and stress fields during TPSF. In this subsection, the propagation path of Fracs. 1&3 under the condition of different formation permeability (0.0001 mD, 0.001 mD, 0.01 mD, 1 mD), are investigated. As shown in Fig. 11, the width of the three fractures decreases with formation permeability, While the length of the three fractures increases. The reason is that leak-off rate is higher in formations with greater formation permeability, which results in less

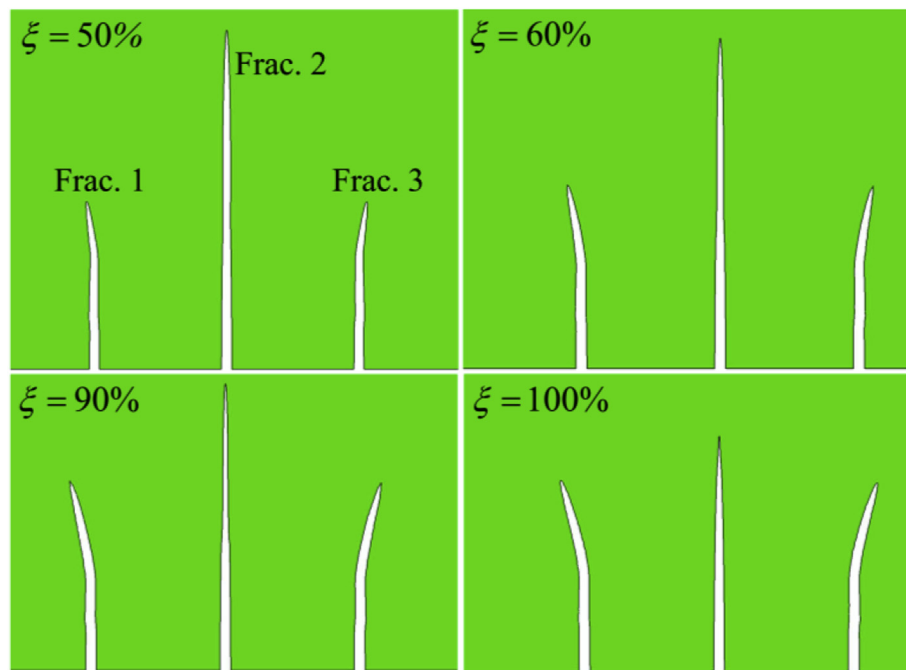


**Fig. 8.** Propagation path and aperture of the three fractures with various plugging efficiency of Frac. 2 (the previous fracture), 300-fold exaggeration of the aperture.  $\xi$  is the plugging efficiency.

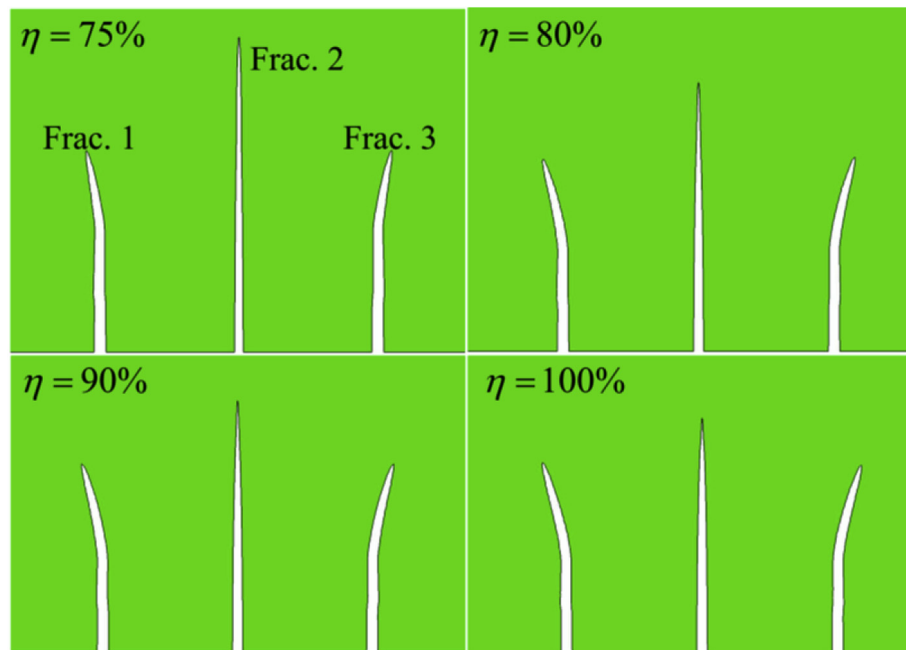


**Fig. 9.** Propagation path and aperture for the three fractures with varying aperture of Frac. 2, 300-fold exaggeration of the aperture.  $\eta$  is the percent of the initial aperture of Frac. 2 propped.

fluid remaining within fracture and lower fluid pressure (Liang et al., 2017b, 2017c), thus generating long and narrow subsequent fractures. Furthermore, Fracs. 1&3 have similar curvatures for cases with different formation permeability, which results from the mutual effects of the low fluid pressure within Fracs. 1&3 and the narrow width of Frac. 2. Fractures with low fluid pressure tend to divert, while the narrow width of Frac. 2 exerts small induced stresses, thus contributes to fracture straight propagation.

### 5.3.3. Horizontal differential stress

In this part, conditions for different horizontal differential stresses

are built by altering the maximum horizontal principal stress, including 2 MPa, 4 MPa, 8 MPa and 10 MPa. Fig. 12 shows the propagation path and aperture of the three fractures with various horizontal differential stresses. It reveals that Fracs. 1&3 propagate with larger curvature as horizontal differential stress increases. The reason is that, as for the four cases, the induced stresses resulting from Frac. 2 are the same, the direction of maximum-circumferential-stress is less influenced for larger horizontal differential stress (Olson and Taleghani, 2009). Thus, Fracs. 1&3 tend to propagate more straightly along the direction of the maximum horizontal stress. Moreover, the width of Fracs. 1&3 is slightly wider for smaller horizontal differential stress. The reason is



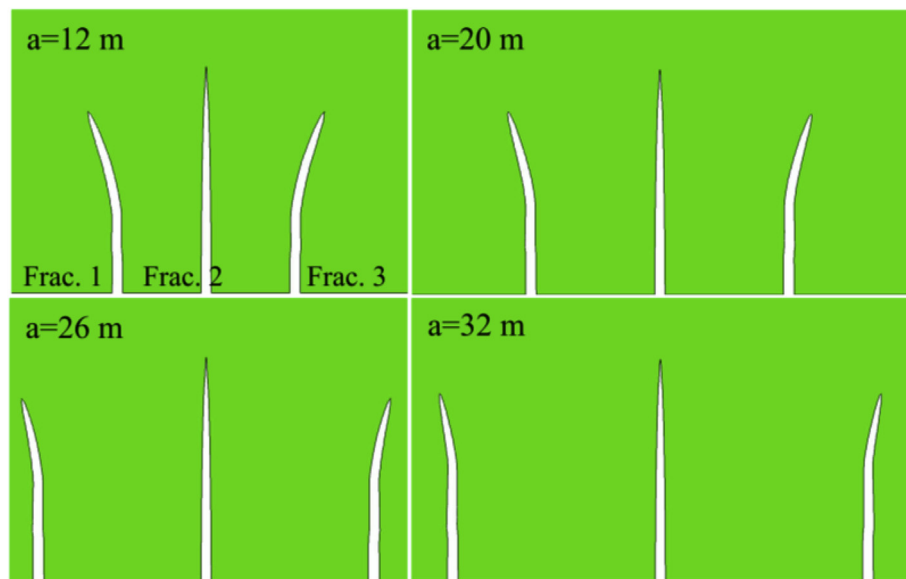


Fig. 10. Propagation path and aperture of the three fractures with varying fracture spacing, 300-fold exaggeration of the apertures,  $a$  is the fracture spacing.

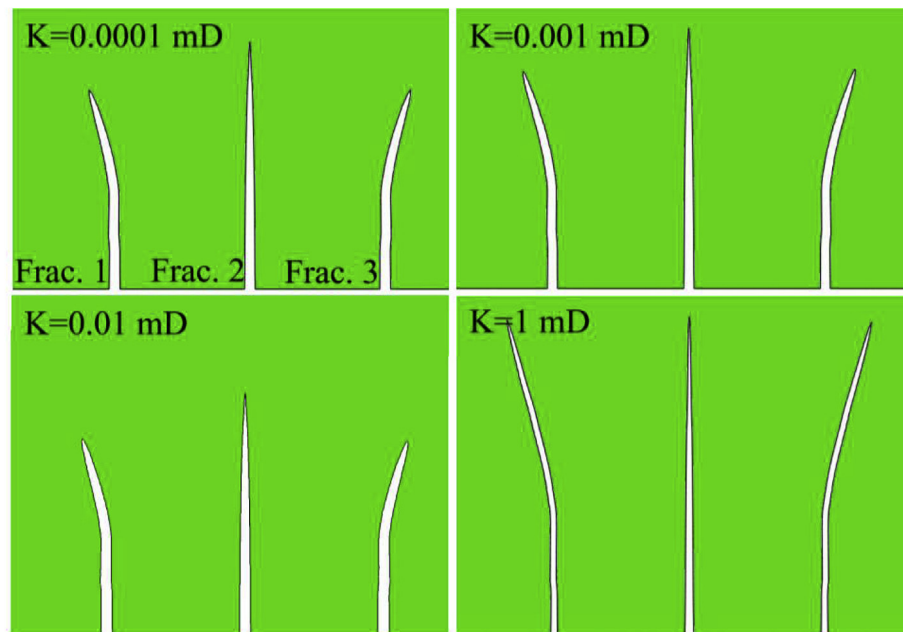


Fig. 11. Propagation path and aperture of the three fractures with varying formation permeability, 300-fold exaggeration of the aperture.  $K$  is the formation permeability.

that greater fracture curvature results in larger propagation resistance, which increases fluid pressure within the fracture and widens the aperture (Li et al., 2017a). Thereby, smaller horizontal differential stress will bring about larger fracture width.

#### 5.4. The effects of rock mechanical parameters in heterogeneous formation

Fracture initiation position, fracture number, and fracture propagation geometry are strongly influenced by formation heterogeneity (Li and Misra, 2017b). This section investigates fracture interaction in heterogeneous formations with a conservative manner through changing the mechanical properties surrounding the subsequent fractures (Fig. 13). Specifically, the rock mechanical properties in Region 2 remain as the base case and those of Regions 1&3 are changed to simulate the formation heterogeneity. This section comprises two parts:

changing Young's modulus and changing the rock tensile strength in Regions 1&3.

##### 5.4.1. Young's modulus

The Young's modulus in Region 2 is remained as 40 GPa. At the end of propagation, Frac. 2 is perfectly plugged and the Young's modulus of Regions 1&3 is changed to 16 GPa, 24 GPa, 32 GPa and 40 GPa, respectively. As shown in Fig. 14, Fracs. 1&3 deviate from Frac. 2 with greater curvature and the aperture becomes smaller with the increase of Young's modulus in Regions 1&3. The reason is that, rock with low Young's modulus generates plastic deformation during propagation, which requires high fluid pressure to propagate fracture (Wang et al., 2016; Yushi et al., 2016). As stated above, high fluid pressure brings about large fracture aperture and promotes Fracs. 1&3 to propagate more straightly.

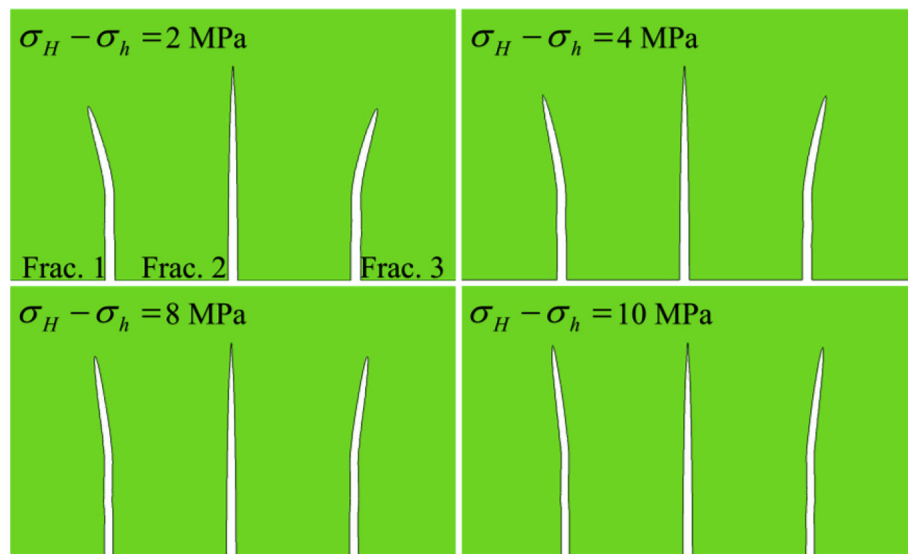


Fig. 12. Propagation path and aperture with different horizontal differential stress, 300-fold exaggeration of the aperture.  $\sigma_H$  is the maximum horizontal principal stress and  $\sigma_h$  is the minimum horizontal principal stress.

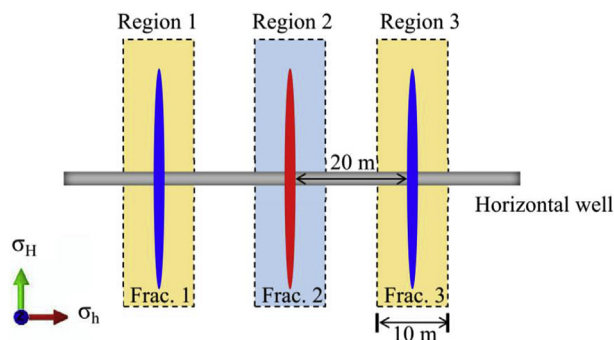


Fig. 13. Approach of processing the formation heterogeneity. Fracture spacing is 20 m and the width of each region is 10 m.

#### 5.4.2. Rock tensile strength

The rock tensile strength of Region 2 remains constant at 2 MPa and the rock tensile strengths of Regions 1&3 are changed to 2 MPa, 4 MPa, 6 MPa and 8 MPa, respectively. The simulation results are presented in Fig. 15. It shows that, with the increase of rock tensile strength in Regions 1&3, Fracs. 1&3 propagate more straightly and have larger fracture aperture. The reason is that larger rock tensile strength gives rise to higher propagation resistance and results in greater fluid pressure within the active fracture (Li et al., 2017b). As stated before, high fluid pressure brings about large fracture aperture and promotes Fracs. 1&3 to propagate more straightly.

## 6. Quantitative analysis of the simulation results

This paper defines a “turning angle” to quantitatively analyze the simulation results. As shown in Fig. 16a, turning angle indicates the

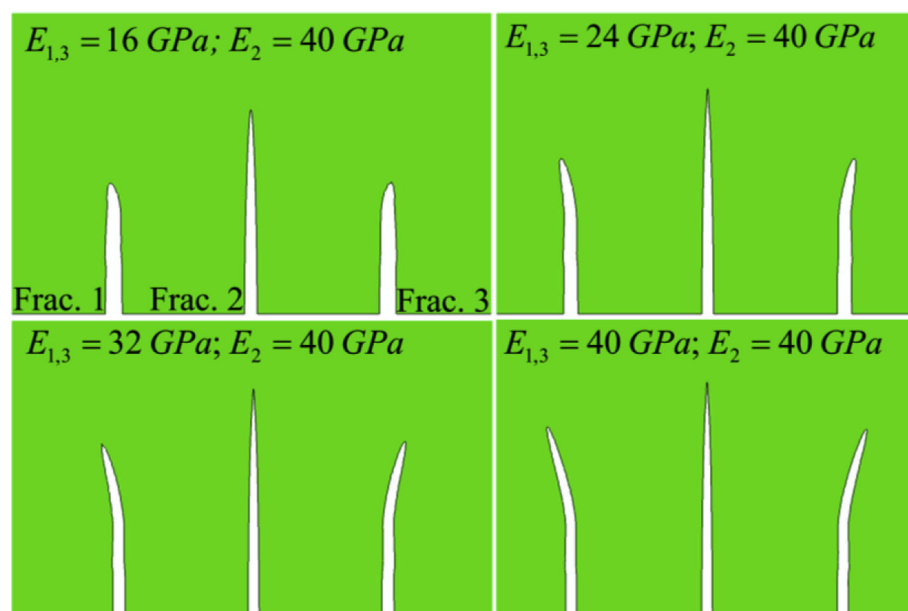


Fig. 14. Propagation path and aperture for the three fractures with different Young's modulus around Fracs. 1&3, 300-fold exaggeration of the aperture.  $E_{1,3}$  is the Young's modulus of Region 1&3.  $E_2$  is the Young's modulus of Region 2.

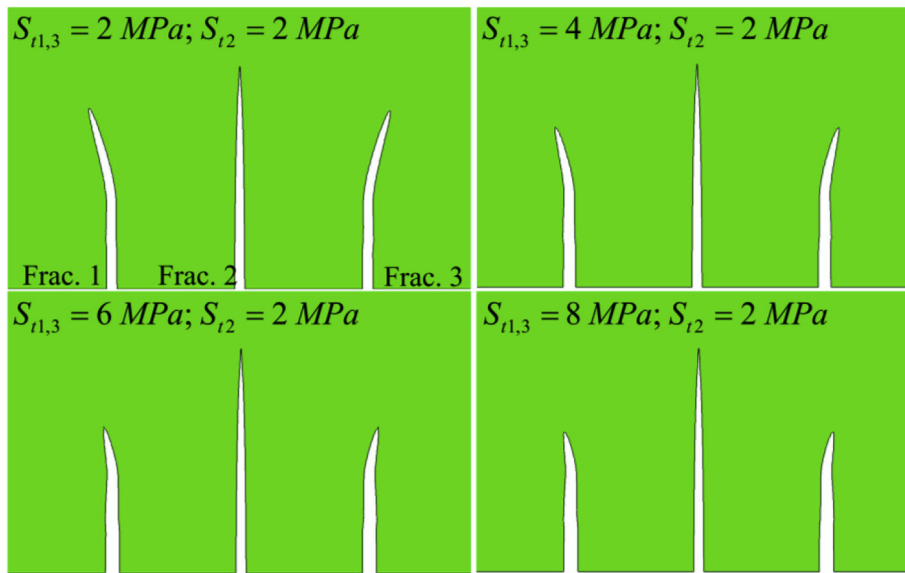


Fig. 15. Propagation path and aperture for the three fractures with different rock tensile strength surrounding Fracs. 1&3, 300-fold exaggeration of the aperture.  $S_{t1,3}$  is the rock tensile strength of Regions 1&3.  $S_{t2}$  is the rock tensile strength of Region 2.

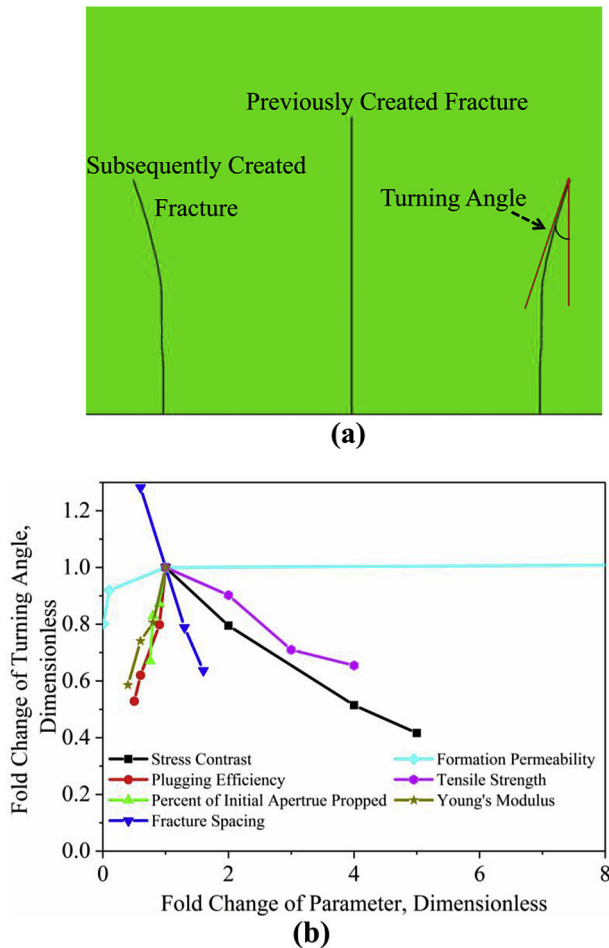


Fig. 16. Quantitative analysis of the simulation results. (a) Definition of turning angle; (b) Fold change of turning angle vs. fold change of the parameter.

angle of Fracs. 1&3 deviating from the initial propagation direction, which indirectly represents the magnitudes of fracture interaction during TPSF. Table 4 lists the specific values of turning angle under different conditions. We define the base case: the horizontal differential

Table 4

Specific values of turning angle for different parameters.

Parameters	Values	Turning Angle (°)	Parameters	Values	Turning Angle (°)
Horizontal	2	20.08	Plugging	50%	10.61
Differential	4	15.96	Efficiency (%)	60%	12.45
Stress (MPa)	8	10.33		90%	16.03
	10	8.36		100%	20.08
Percent of Initial	100%	20.08	Fracture	12	25.74
Aperture	90%	17.51	Spacing (m)	20	20.08
Propped (%)	80%	16.65		26	15.83
	75%	13.46		32	12.78
Formation	0.0001	16.08	Rock Tensile	2	20.08
Permeability	0.001	18.46	Strength	4	18.12
(mD)	0.01	20.08	(MPa)	6	14.25
	1	22.45		8	13.14
Young's Modulus	16	11.76			
(GPa)	24	14.87			
	32	16.19			
	40	20.08			

Table 5

Association degree between the parameter and turning angle.

stress contrast	Plugging efficiency	Percent of initial aperture propped	Fracture spacing	Formation permeability	Rock tensile strength	Young's modulus
0.9343	0.9632	0.9603	0.9482	0.9249	0.9275	0.9605

stress of 2 MPa, plugging efficiency of 100%, 100% of initial aperture propped, fracture spacing of 20 m, formation permeability of 0.01 mD, rock tensile strength of 2 MPa, and Young's modulus of 40 GPa. The turning angle obtained from the base case is 20.08°. The specific values of turning angle in Table 4 are normalized by the values in the base case, respectively. The relationship between fold change of turning angle vs. fold change of parameter is presented in Fig. 16b. Further, we use the grey relative analysis method (Hou, 2013) to determine the major factors influencing fracture interaction. The association degrees between the parameter and turning angle were calculated and listed in Table 5. Both from Fig. 16b and Table 5, we can conclude that the

influencing factors can be sorted by sensitivity: plugging efficiency, Young's modulus, percent of initial aperture propped, fracture spacing, horizontal stress contrast, rock tensile strength, and formation permeability.

The input parameters used in the simulations were prescribed based on a typical unconventional reservoir. Changing the magnitudes of input parameters may result in different magnitudes of turning angle, while the influence tendency of various factors is suitable for all reservoirs.

## 7. Conclusions

Fracture interaction was investigated quantitatively and systematically through numerical simulation. The conclusions are as follows:

- (1) Propped fracture and fluid pressure generate extra stresses, which alter the initial stress fields and affect the propagation curvature and width of subsequent fractures. High horizontal stress, large formation permeability, and large fracture spacing will weaken the fracture interaction. Moreover, efficiently plugging the previous fracture will promote uniform propagation of multiple fractures.
- (2) Subsequent fracture created in the region with high rock tensile strength and low Young's modulus will propagate more straightly and generate wider apertures. The greater the difference of mechanical property between the previous fracture region and the subsequent fracture region, the more uneven propagation of the previous fracture and the subsequent fracture. TPSF is more applicable in formations with smaller heterogeneity because the injection pressures of the previous fracture and the subsequent fracture are more close and lower plugging efficiency is required to initiate and propagate multiple fractures.
- (3) By comparing the subsequent fracture propagation curvature, factors influencing fracture interaction during TPSF can be sorted by sensitivity (strong to weak): plugging efficiency, Young's modulus, percent of initial aperture propped, fracture spacing, horizontal stress contrast, rock tensile strength, and formation permeability.

## Acknowledgments

The authors give their sincere gratitude to Dassault Systemes Simulia Corporation for providing ABAQUS software program. This work is financially supported by the Foundation of State Key Laboratory of Petroleum Resources and Prospecting (Grant No. PRP/indep-4-1703), the National Science Foundation of China (51804033), the National Science and Technology Major Projects of China (Grant Nos. 2016ZX05051 and 2017ZX05030), PetroChina Innovation Foundation (2018D-5007-0205), the Science Foundation of China University of Petroleum at Beijing (Grant No. 2462017YJRC031), the Beijing Postdoctoral Research Foundation (2018-ZZ-045).

## References

Abass, H.H., Brumley, J.L., Venditto, J.J., 1994, January 1. Oriented Perforations - A Rock Mechanics View. Society of Petroleum Engineers <https://doi.org/10.2118/28555-MS>.  
 Allison, D.B., Curry, S.S., Todd, B.L., 2011, January 1. Restimulation of Wells Using Biodegradable Particulates as Temporary Diverting Agents. Society of Petroleum Engineers <https://doi.org/10.2118/149221-MS>.  
 Aviles, I., Dardis, M., Jacob, G., 2015, June 1. Dissolvable Plug and Perf System Eliminates Mill-outs in Multistage Stimulations. Society of Petroleum Engineers <https://doi.org/10.2118/0615-0038-JPT>.  
 Belytschko, T., Black, T., 1999. Elastic crack growth in finite elements with minimal remeshing. *Int. J. Numer. Meth. Eng.* 45 (5), 601–620.  
 Benzeggagh, M.L., Kenane, M., 1996. Measurement of mixed-mode delamination fracture toughness of unidirectional glass/epoxy composites with mixed-mode bending apparatus. *Compos. Sci. Technol.* 56 (4), 439–449.  
 Cheng, W., Jiang, G., Jin, Y., 2017. Numerical simulation of fracture path and nonlinear closure for simultaneous and sequential fracturing in a horizontal well. *Comput. Geotech.* 88, 242–255.

Dahi-Taleghani, A., Olson, J.E., 2011. Numerical modeling of multi-stranded hydraulic fracture propagation: accounting for the interaction between induced and natural fractures. *SPE J.* 16 (3), 575–581.  
 Dahi Taleghani, A., Olson, J.E., 2014. How natural fractures could affect hydraulic fracture geometry. *SPE J.* 19 (01), 161–171.  
 Fries, T., Baydoun, M., 2012. Crack propagation with the extended finite element method and a hybrid explicit-implicit crack description. *Int. J. Numer. Meth. Eng.* 89 (12), 1527–1558.  
 Feng, Y., Arlanoglu, C., Podnos, E., Becker, E., Gray, K.E., 2015. Finite-element studies of hoop-stress enhancement for wellbore strengthening. *SPE Drill. Complet.* 30 (01), 38–51.  
 Feng, Y., Jones, J.F., Gray, K.E., 2016. A review on fracture-initiation and-propagation pressures for lost circulation and wellbore strengthening. *SPE Drill. Complet.* 31 (02), 134–144.  
 Feng, Y., Gray, K.E., 2017. Parameters controlling pressure and fracture behaviors in field injectivity tests: a numerical investigation using coupled flow and geomechanics model. *Comput. Geotech.* 87, 49–61.  
 Gensheng, L.L., Sheng, M., Tian, S., Huang, Z., Yuanbin, L.L., Yuan, X., 2012. Multistage hydraulic jet acid fracturing technique for horizontal wells. *Petrol. Explor. Dev.* 39 (1), 107–112.  
 Gomaa, A.M., Nino-Penaloza, A., Castillo, D., McCartney, E., Mayor, J., 2016a. Experimental Investigation of Particulate Diverters Used to Enhance Fracture Complexity. Society of Petroleum Engineers <https://doi.org/10.2118/178983-MS>.  
 Gomaa, A.M., Nino-Penaloza, A., McCartney, E., Mayor, J., 2016b. Engineering Solid Particulate Diverters to Control Fracture Complexity: *Experimental Study*. Society of Petroleum Engineers <https://doi.org/10.2118/179144-MS>.  
 Haddad, M., Sepehrmoori, K., 2014, May). Cohesive fracture analysis to model multiple-stage fracturing in quasibrittle shale formations. In: 2014 SIMULIA Community Conference, Providence, Rhode Island, USA, pp. 506–520.  
 Haddad, M., Sepehrmoori, K., 2016. XFEM-based CZM for the simulation of 3D multiple-cluster hydraulic fracturing in quasi-brittle shale formations. *Rock Mech. Rock Eng.* 49 (12), 4731–4748.  
 Hou, J., 2013. Grey relational analysis method for multiple attribute decision making in intuitionistic fuzzy setting. *J. Convergence. Inf. Technol.* 5 (10), 194–199.  
 Kresse, O., Cohen, C., Weng, X., Wu, R., Gu, H., 2011, January 1. Numerical Modeling of Hydraulic Fracturing in Naturally Fractured Formations. American Rock Mechanics Association.  
 Li, H., Misra, S., 2017a. Assessment of miscible light-hydrocarbon-injection recovery efficiency in bakken shale formation using wireline-log-derived indices. *Mar. Petrol. Geol.* 89.  
 Li, H., Misra, S., 2017b. Prediction of subsurface NMR T2 distributions in a shale petroleum system using variational autoencoder-based neural networks. *Geosci. Rem. Sens. Lett. IEEE PP(99)*, 1–3.  
 Li, Y., Deng, J., Liu, W., Yan, W., Feng, Y., Cao, W., et al., 2017a. Numerical simulation of limited-entry multi-cluster fracturing in horizontal well. *J. Petrol. Sci. Eng.* 152, 443–455.  
 Li, Y., Deng, J.G., Liu, W., Feng, Y., 2017b. Modeling hydraulic fracture propagation using cohesive zone model equipped with frictional contact capability. *Comput. Geotech.* 91, 58–70.  
 Liang, T., Longoria, R.A., Lu, J., Nguyen, Q.P., DiCarlo, D.A., 2017a. Enhancing hydrocarbon permeability after hydraulic fracturing: laboratory evaluations of shut-ins and surfactant additives. *SPE J.* 22 (1). <https://doi.org/10.2118/175101-PA>. 011–1,023.  
 Liang, T., Luo, X., Nguyen, Q., DiCarlo, D.A., 2017b. Computed-tomography measurements of water block in low-permeability rocks: scaling and remedying production impairment. *SPE J.* <https://doi.org/10.2118/189445-PA>.  
 Liang, T., Zhou, F., Lu, J., DiCarlo, D., Nguyen, Q., 2017c. Evaluation of wettability alteration and IFT reduction on mitigating water blocking for low-permeability oil-wet rocks after hydraulic fracturing. *Fuel* 209, 650–660. <https://doi.org/10.1016/j.fuel.2017.08.029>.  
 Liu, C., Liu, H., Zhang, Y., Deng, D., Wu, H., 2015. Optimal spacing of staged fracturing in horizontal shale-gas well. *J. Petrol. Sci. Eng.* 132, 86–93.  
 Liu, C., Shi, F., Zhang, Y., Zhang, Y., Deng, D., Wang, X., Wu, H., 2017. High injection rate stimulation for improving the fracture complexity in tight-oil sandstone reservoirs. *J. Nat. Gas Sci. Eng.* 42, 133–141.  
 Liu, Z., Forouzanfar, F., 2017. Ensemble clustering for efficient robust optimization of naturally fractured reservoirs. *Comput. Geosci.* (2), 1–14.  
 Meyer, B.R., Bazan, L.W., 2011, January 1. A Discrete Fracture Network Model for Hydraulically Induced Fractures - Theory, Parametric and Case Studies. Society of Petroleum Engineers <https://doi.org/10.2118/140514-MS>.  
 Nagel, N.B., Sanchez-Nagel, M.A., Zhang, F., Garcia, X., Lee, B., 2013. Coupled numerical evaluations of the geomechanical interactions between a hydraulic fracture stimulation and a natural fracture system in shale formations. *Rock Mech. Rock Eng.* 46 (3), 581–609.  
 Olson, J.E., Taleghani, A.D., 2009, January 1. Modeling Simultaneous Growth of Multiple Hydraulic Fractures and Their Interaction with Natural Fractures. Society of Petroleum Engineers <https://doi.org/10.2118/119739-MS>.  
 Potapenko, D.I., Tinkham, S.K., Lecerf, B., Fredd, C.N., Samuelson, M.L., Gillard, M.R., Daniels, J.L., 2009, January 1. Barnett Shale Refracture Stimulation Using a Novel Diversion Technique. Society of Petroleum Engineers <https://doi.org/10.2118/119636-MS>.  
 Rahim, Z., Al-Kanaan, A., Taha, S., Crawford, E.M., Khalifa, M., Krich, D., Lahman, M., 2017, January 24. Innovative Diversion Technology Ensures Uniform Stimulation Treatments and Enhances Gas Production: Example from Carbonate and Sandstone Reservoirs. Society of Petroleum Engineers <https://doi.org/10.2118/184840-MS>.  
 Rytlewski, G. L., Morales, H., Gadiyar, B., Lassek, J., Whitsitt, J. R., de Cardenas, J. L., & Hackworth, M. R. (2008). U.S. Patent Application No. 12/058,062.



- Senters, C.W., Johnson, M.D., Leonard, R.S., Ramos, C.R., Squires, C.L., Wood, T.M., Woodroof, R.A., 2018, January 23. Diversion Optimization in New Well Completions. Society of Petroleum Engineers <https://doi.org/10.2118/189900-MS>.
- Wang, B., Zhou, F., Wang, D., Liang, T., Yuan, L., Hu, J., 2018. Numerical simulation on near-wellbore temporary plugging and diverting during refracturing using xfem-based czm. *J. Nat. Gas Sci. Eng.*
- Wang, D., Zhou, F., Ge, H., Shi, Y., Yi, X., Xiong, C., et al., 2015a. An experimental study on the mechanism of degradable fiber-assisted diverting fracturing and its influencing factors. *J. Nat. Gas Sci. Eng.* 27, 260–273.
- Wang, D., Zhou, F., Ding, W., Ge, H., Jia, X., Shi, Y., et al., 2015b. A numerical simulation study of fracture reorientation with a degradable fiber-diverting agent. *J. Nat. Gas Sci. Eng.* 25, 215–225.
- Wang, H., Soliman, M.Y., Towler, B.F., 2009, September 1. Investigation of Factors for Strengthening a Wellbore by Propping Fractures. Society of Petroleum Engineers <https://doi.org/10.2118/112629-PA>.
- Wang, X., Liu, C., Wang, H., Liu, H., Wu, H., 2016. Comparison of consecutive and alternate hydraulic fracturing in horizontal wells using XFEM-based cohesive zone method. *J. Petrol. Sci. Eng.* 143, 14–25.
- Weddle, P., Griffin, L., Pearson, C.M., 2017, January 24. Mining the Bakken: Driving Cluster Efficiency Higher Using Particulate Diverters. Society of Petroleum Engineers <https://doi.org/10.2118/184828-MS>.
- Weng, X., Kresse, O., Cohen, C.-E., Wu, R., Gu, H., 2011, November 1. Modeling of Hydraulic-fracture-network Propagation in a Naturally Fractured Formation. Society of Petroleum Engineers <https://doi.org/10.2118/140253-PA>.
- Wu, K., Olson, J.E., 2013, November 1. Investigation of the Impact of Fracture Spacing and Fluid Properties for Interfering Simultaneously or Sequentially Generated Hydraulic Fractures. Society of Petroleum Engineers <https://doi.org/10.2118/163821-PA>.
- Wu, K., Olson, J.E., 2015, April 1. Simultaneous Multifracture Treatments: Fully Coupled Fluid Flow and Fracture Mechanics for Horizontal Wells. *Society of Petroleum Engineers* <https://doi.org/10.2118/167626-PA>.
- Wu, K., Olson, J.E., 2016, June 1. Mechanisms of Simultaneous Hydraulic-fracture Propagation from Multiple Perforation Clusters in Horizontal Wells. Society of Petroleum Engineers <https://doi.org/10.2118/178925-PA>.
- Wu, K., Olson, J., Balhoff, M.T., Yu, W., 2017, February 1. Numerical Analysis for Promoting Uniform Development of Simultaneous Multiple-fracture Propagation in Horizontal Wells. Society of Petroleum Engineers <https://doi.org/10.2118/174869-PA>.
- Wu, R., Kresse, O., Weng, X., Cohen, C.-E., Gu, H., 2012, January 1. Modeling of Interaction of Hydraulic Fractures in Complex Fracture Networks. Society of Petroleum Engineers <https://doi.org/10.2118/152052-MS>.
- Xu, W., Thiercelin, M.J., Ganguly, U., Weng, X., Gu, H., Onda, H., Le Calvez, J., 2010, January 1. Wiremesh: a Novel Shale Fracturing Simulator. Society of Petroleum Engineers <https://doi.org/10.2118/132218-MS>.
- Yushi, Z., Xinfang, M., Shicheng, Z., Tong, Z., Han, L., 2016. Numerical investigation into the influence of bedding plane on hydraulic fracture network propagation in shale formations. *Rock Mech. Rock Eng.* 49 (9), 3597–3614.
- Yushi, Z., Xinfang, M., Tong, Z., Ning, L., Ming, C., Sihai, L., Han, L., 2017. Hydraulic fracture growth in a layered formation based on fracturing experiments and discrete element modeling. *Rock Mech. Rock Eng.* 1–15.
- Zhang, G.M., Liu, H., Zhang, J., Wu, H.A., Wang, X.X., 2010. Three-dimensional finite element simulation and parametric study for horizontal well hydraulic fracture. *J. Petrol. Sci. Eng.* 72 (3), 310–317.
- Zielonka, M.G., Searles, K.H., Ning, J., et al., 2014. Development and validation of fully-coupled hydraulic fracturing simulation capabilities. In: Pre-sented at the 2014 SIMULIA Community Conference, Providence, Rhode Island.
- Zou, Y., Zhang, S., Ma, X., Zhou, T., Zeng, B., 2016. Numerical investigation of hydraulic fracture network propagation in naturally fractured shale formations. *J. Struct. Geol.* 84, 1–13.